Progress In Electromagnetics Research, Vol. 130, 105–130, 2012

POLARIMETRIC SAR TOMOGRAPHY USING $\ell_{2,1}$ MIXED NORM SPARSE RECONSTRUCTION METHOD

S. Xing*, D. Dai, Y. Li, and X. Wang

School of Electronic Science and Engineering, National University of Defense Technology, Changsha 410073, China

Abstract—The growing interest of Radar community in retrieving the 3D reflectivity map makes both polarimetric SAR interferometry and SAR tomography hot topics in recent years. It is expected that combining these two techniques would provide much better discriminating ability for scatterers lying in the same pixel. Generally, this is about reconstruction of scattering profiles from limited and irregular polarimetric measurements. As an emerging technique, Compressive Sensing (CS) provides a powerful tool to achieve the purpose. In this paper, we propose a $\ell_{2,1}$ mixed norm sparse reconstruction method for jointly processing multibaseline PolInSAR data based on *multiple measurement vector compressive sensing* (MMV-CS) model, and also address the signal leakage problem with MMV-CS inversion by presenting a window based iterative algorithm. The results obtained by processing simulated data show that the proposed method possesses superior performance advantage over existing methods.

1. INTRODUCTION

Synthetic Aperture Radar (SAR) systems provide the full ability of acquiring high resolution radar images independent of sunlight illumination and weather conditions [1–4]. Conventional SAR provides the 2D projected scene reflectivity map. The unwelcome effects like layover and foreshortening, induced by the projection from 3D space to 2D plane, seriously handicap the understanding and interpretation of SAR image, especially in the urban areas [4, 5]. Assuming the scattering occurs only on the surface, interferometric SAR measures

Received 14 May 2012, Accepted 6 July 2012, Scheduled 27 July 2012

* Corresponding author: Shiqi Xing (xingshiqi_paper@163.com).

the ground height [6–10]. However, it can not resolve multiple scatterers lying in single pixel. In addition, the interferometric quality will be seriously deteriorated by volume scattering effect, and the phase unwrapping techniques may not work for man made structures [11]. Polarimetric interferometric theory and the model based *polarimetric coherence tomography* (PCT) technique have demonstrated their discrimination ability for scatterers of different scattering mechanism in the vegetation structure inversion application [12]. There still exist no polarimetric interferometric techniques that can be applied in a more general case, such as the reconstruction of man made target.

SAR tomography, first introduced in 1990s, is aimed to retrieve the real 3D reflectivity distribution along range, azimuth and elevation directions using multi-acquisition data [13], and have been inspired by the new launched high resolution SAR satellites, e.g., TerraSAR, COSMO-Skymed. Recent published studies demonstrate the great potential of SAR tomography in urban infrastructure monitoring [14–18], vehicle detection and reconstruction [19, 20], and forest structure inversion [21, 22], etc.. Generally, SAR tomography can be formulated as a 3D reconstruction problem in the wave number domain, or factorized as a 2D conventional SAR processing scheme plus a following 1D parameter estimation stage. The latter strategy is more preferred by researchers due to its superior efficiency, and we will concentrate on it in this study.

Tomographic SAR data are usually characterized by small angular diversity, limited acquisition number, and maybe irregular sensor geometry. And practical systems are always forced to make a compromise between the Fourier resolution (be determined by the angular diversity) and the ambiguity height (be determined by the sensor space). Therefore, the performance of inversion algorithm, especially regarding the super resolution power and ambiguity suppression ability, is of great significance. Various algorithms are proposed for SAR tomography, e.g., Fourier beamforming, MUSIC, ESPRIT, Capon, TSVD, and Compressive Sensing (CS) methods. Without loss of generality, they can be recognized as methods with or without multilook processing. When man made targets are confronted, the latter kind techniques seem to be more attractive, since they well preserve the radar resolution which is very important to the understanding of the image of man made structures. The TSVD and CS techniques all belong to this kind. Compared to TSVD, CS methods exhibit much lower ambiguity level and significantly finer super resolution ability [16, 17]. Nevertheless, CS techniques also show some serious drawback like signal leakage problem (see, e.g., [23–26] and our later discussion).

Noting the discrimination ability of polarimetric information itself, it is expected that polarimetric measurements would help to refine tomographic results. In [21], the forest tomography dependence on polarization is investigated. In [19], it is reported that the reconstruction of a hidden truck beneath foliage is greatly improved by utilizing multi-polarimetric data. Conventionally, data for different polarimetric channels are processed separately, and then fused together for more information. This processing scheme may reduce the accuracy and robustness of the parameter estimation, and poses another challenge, i.e., matching the scatterers in different channels. In [18], some multilook data based algorithms, including MUSIC and Capon, etc., are extended to polarimetric case. In [27], distributed compressive sensing technique (DCS) is introduced in SAR tomography, and the authors successfully realize the separation of two corner reflectors in the height direction using multi-polarization data.

In this paper, we propose a tomography method for jointly processing multibaseline PolInSAR data, following the idea of compressive sensing. The technique consists of two major parts, which are the $\ell_{2,1}$ mixed norm sparse reconstruction method, and a window based iterative signal leakage suppression algorithm, respectively. We consider both the uniform and nonuniform baseline distribution in such a way as to comprehensively evaluate the performance of the proposed reconstruction algorithm, and the most relevant conclusion in our paper is that the proposed method possesses superior performance advantage over existing methods.

The paper is organized as follows: In Section 2, the principle of SAR tomography is briefly recalled, and the polarimetric data model is established; Section 3 formulates the PolSAR tomography problem as a mixed norm minimization problem in the CS framework. Also a window-based algorithm to suppress the signal leakage is introduced and described; In Section 4, simulations are presented to verify the effectiveness of our algorithm.

2. BASIC PRINCIPLE AND DATA MODEL

The basic idea of SAR tomography is to obtain the height resolution by forming an additional aperture along the direction perpendicular to the range and azimuth directions. Consider the data acquisition geometry shown in Fig. 1. The SAR sensors illuminate the area of interest from M slightly different looking angles, and receive the signal scattered by the scene. In practice, these data can be provided by either multipass system or multi-channels of single pass system. When all acquisition data are focused into complex images and the images are

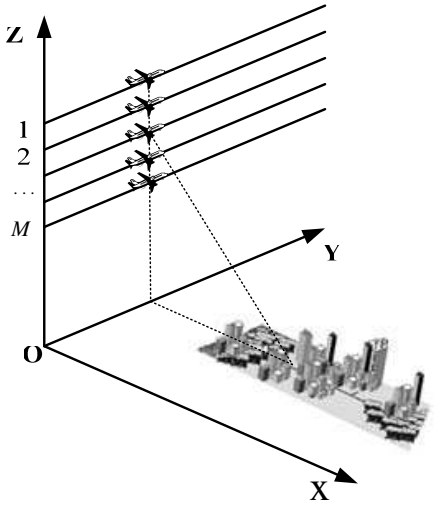

Figure 1. The data acquisition geometry of tomography SAR. The vertical synthetic aperture is formed by M tracks for multipass system or M antennas for single pass system. The sensors are located in the same plane perpendicular to the moving direction. However the sensor separations are not necessarily uniform.

co-registered, SAR tomography can be reduced into a one dimensional inversion problem in the elevation direction.

We denote with P_m, $b_m^{\parallel}$ and $b_m^{\perp}$ the mth sensor position, the space between the mth sensor and the reference sensor along the LOS and PLOS, respectively (see Fig. 2). Assuming a fixed range and azimuth pixel, the signal in the image produced by the mth sensor is the superstition of signals from multiple scatterers located in the pixel. For the polarimetric case, this can be formulated as

$$g_{pq}^{m}(r_0, y) = \int_{-L_1/2}^{L_1/2} \boldsymbol{\gamma}_{pq}(r_0, y, s) \exp(-j4\pi R_m(s)/\lambda)\, ds \qquad (1)$$

where λ denotes the carrier wavelength; (r_0, y, s) defines the fixed target position in the range-azimuth-elevation coordinate system; L_1 denotes the target extent along the PLOS direction; pq represents the specific polarimetric choice from $\{HH,\ HV,\ VH,\ VV\}$; $\boldsymbol{\gamma}$ is the reflectivity function. The path between the mth sensor and the target is denoted with $R_m(s)$ and can be approximated as (see Fig. 2 for the geometry)

$$R_m(s) = \sqrt{\left(r_0 + b_m^{\parallel}\right)^2 + \left(b_m^{\perp} - s\right)^2} \cong r_0 + b_m^{\parallel} + \frac{\left(b_m^{\perp} - s\right)^2}{2r_0} \qquad (2)$$

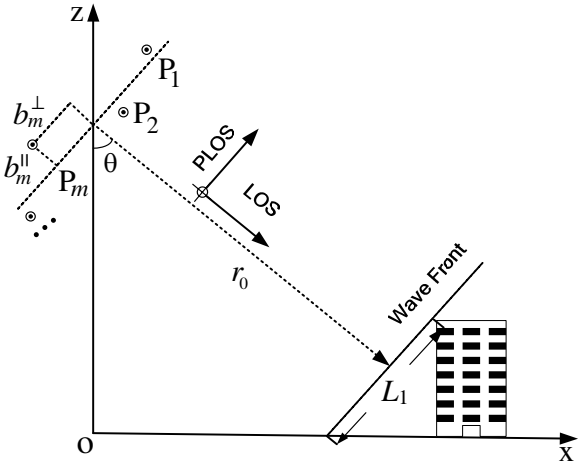

Figure 2. The geometry of SAR tomography with reduced dimensions. PLOS and LOS refer to the directions perpendicular and parallel to line of sight, respectively.

Hence, the phase term in (1) induced by the two way path travel is

$$\varphi = -\frac{4\pi}{\lambda}\left(r_0 + b_m^{\parallel} + \frac{\left(b_m^{\perp} - s\right)^2}{2r_0}\right) = -\frac{4\pi}{\lambda}\left(r_0 + b_m^{\parallel} + \frac{b_m^{\perp 2}}{2r_0} + \frac{s^2}{2r_0} - \frac{b_m^{\perp} s}{r_0}\right) \quad (3)$$

We note that the first three terms in bracket of (3) are target independent and can be eliminated by a well-known technique named deramping [4]. And the fourth term, known as residual phase, can be absorbed into the reflectivity function. Thus, for a fixed pixel, the signal after deramping can be modeled as

$$g_{pq}^{m} = \int_{-L_1/2}^{L_1/2} \boldsymbol{\gamma}_{pq}(s) \exp\left(j2\pi\omega_m s\right) ds \quad (4)$$

where $\omega_m = 2b_m^{\perp}/(\lambda r_0)$. Eq. (4) shows that the signal g_{pq}^{m} is the Fourier Transform sample of the reflectivity function. It follows from (4) that, when using FFT to recover $\boldsymbol{\gamma}_{pq}(s)$, the elevation resolution and the ambiguity value are

$$\rho_e = \lambda r_0 / 2L \quad (5)$$

$$h_e = \lambda r_0 / 2\Delta b \quad (6)$$

where L denotes the total baseline span along the PLOS, and Δb denotes the sensor separation. The constraint on the sensor separation are given by

$$|\Delta\omega_m| = |\omega_m - \omega_{m-1}| \leq 1/L_a \quad (7)$$

Combining (5) and (7) tells the minimum acquisition number

$$M_{\min} = 2LL_a/\lambda r_0 \tag{8}$$

However, (5)–(8) can only serve as references for performance comparison, since neither the resolution nor the sensor separation requirement is imperative when we come to CS inversion technique. Sampling $\boldsymbol{\gamma}_{pq}$ at N points s_n $(1 \leq n \leq N)$ equal spaced by ε_s, rewriting (4) in the discrete form, and then taking noise into consideration yields

$$\mathbf{g} = \mathbf{A}\boldsymbol{\gamma} + \mathbf{n} \tag{9}$$

where $\mathbf{A}$ is the partial Fourier transform operator $(M \times N)$ with $\mathbf{A}_{mn} = \exp(j2\pi\omega_m s_n)$, and $\mathbf{n}$ is noise matrix $(M \times 4)$ with power σ^2. The other variables are defined as follows

$$\mathbf{g} = \begin{bmatrix} \mathbf{g}_{HH} & \mathbf{g}_{HV} & \mathbf{g}_{VH} & \mathbf{g}_{VV} \end{bmatrix} \tag{10}$$

$$\boldsymbol{\gamma} = \begin{bmatrix} \boldsymbol{\gamma}_{HH} & \boldsymbol{\gamma}_{HV} & \boldsymbol{\gamma}_{VH} & \boldsymbol{\gamma}_{VV} \end{bmatrix} \tag{11}$$

$$\mathbf{g}_{pq} = \begin{bmatrix} \mathbf{g}_{pq}^1 & \mathbf{g}_{pq}^2 & \cdots & \mathbf{g}_{pq}^M \end{bmatrix}^{\mathrm{T}} \tag{12}$$

$$\boldsymbol{\gamma}_{pq} = \begin{bmatrix} \boldsymbol{\gamma}_{pq}^1 & \boldsymbol{\gamma}_{pq}^2 & \cdots & \boldsymbol{\gamma}_{pq}^N \end{bmatrix}^{\mathrm{T}} \tag{13}$$

To allow super resolution performance, $\boldsymbol{\gamma}_{pq}$ is usually sampled very densely, hence $N \gg M$ in most cases, implying that (9) is under determinate. Therefore, to find appropriate solution, additional constraint should be applied. A widely used strategy is to find the minimum energy solution (see the following discussion), but recent studies show the largest sparsity criterion is more appropriate to SAR tomography, and we will discuss it in the next section.

3. TOMOGRAPHIC METHOD

This section formulates the PolSAR tomography problem in the CS framework, and investigates the choice of the mixed norm involved in the CS inversion technique. The signal leakage problem is introduced and then addressed with a window-based iterative algorithm.

3.1. PolSAR Tomography in CS Framework

The most attractive idea of CS is that it is very possible to recover a signal sampled at a much lower rate than Nyquist rate, if it is sparse in an *apriori* known basis [28, 29]. When we say a signal is sparse, it means the signal can be represented as a linear combination of just a few elements from a known basis $\boldsymbol{\Phi}$. The sparsity assumption is well satisfied for SAR tomography, where the scattered signal can be

approximated by several point-like scatterers' responses (see, e.g., [15] for more discussion). The basis matrix $\mathbf{\Phi}$ in SAR tomography is often chosen to be identity matrix $\mathbf{I}$, which provides the best *mutual incoherence property* (*MIP*) with the sensing matrix $\mathbf{A}$.

In polarimetric case, it should be stressed that the signal are jointly sparse in different channels, that is, the indices of the nonzero entries are independent of the polarization. Mathematically, the CS polarimetric tomography can be formulated as a *multiple measurements vector* (MMV) problem [30], i.e.,

$$\min \|\boldsymbol{\gamma}\|_{u,0} \quad \text{s.t.} \quad \|\text{vec}\,(\mathbf{g} - \mathbf{A}\boldsymbol{\gamma})\|_2^2 \leq \varepsilon^2 \tag{14}$$

where vec() denotes the vectorization operation, ε accounts for the

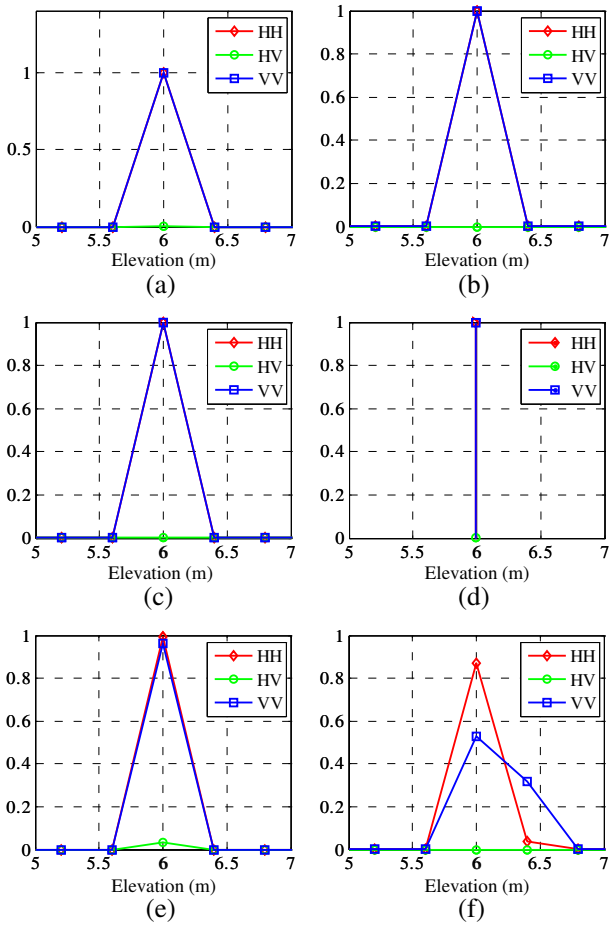

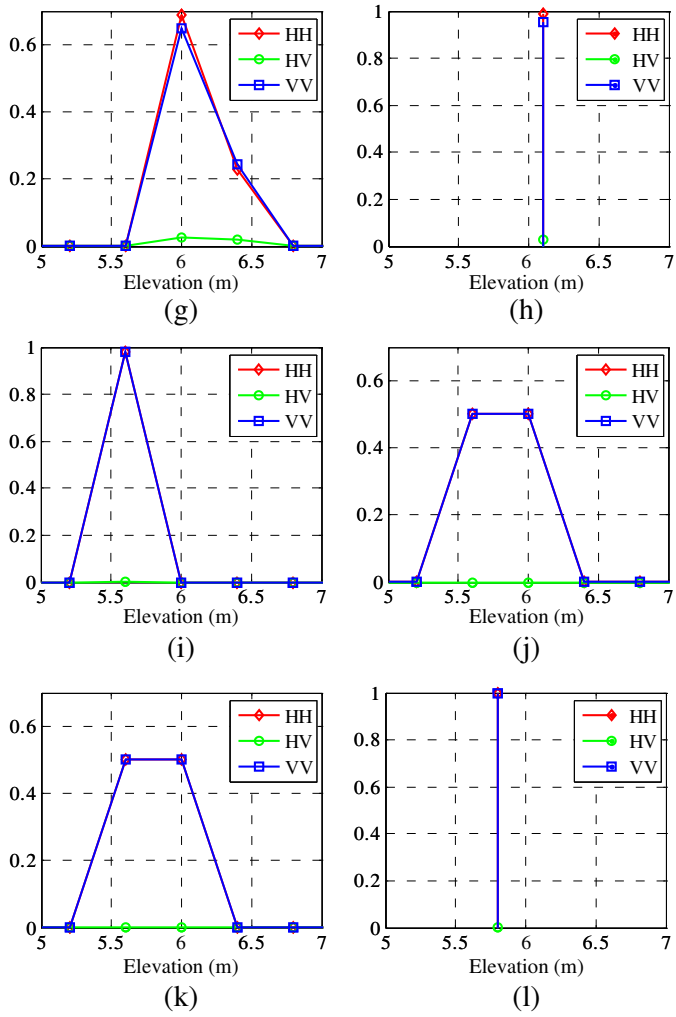

Figure 3. The elevation profiles of a single scatterer obtained with CS tomography techniques. Three cases are examined. Case 1: noise free, and the scatterer lying exactly at the gridding point; Case 2: SNR = 15 dB and the scatterer lying exactly at the gridding point; Case 3: noise free, but the scatterer is away from at the gridding point. (a) M-OMP, case 1. (b) $\ell_{1,1}$ norm, case 1. (c) $\ell_{2,1}$ norm, case 1. (d) $\ell_{2,1}$ norm with SLS, case 1. (e) M-OMP, case 2. (f) $\ell_{1,1}$ norm, case 2. (g) $\ell_{2,1}$ norm, case 2. (h) $\ell_{2,1}$ norm with SLS, case 2. (i) M-OMP, case 3. (j) $\ell_{1,1}$ norm, case 3. (k) $\ell_{2,1}$ norm, case 3. (l) $\ell_{2,1}$ norm with SLS, case 3.

noise, and the mixed norm $\ell_{u,v}$ is defined as

$$\|\boldsymbol{\gamma}\|_{u,v} = \|\boldsymbol{\beta}\|_v, \qquad \boldsymbol{\beta} = \left(\left\|\boldsymbol{\gamma}^1\right\|_u, \quad \left\|\boldsymbol{\gamma}^2\right\|_u, \quad \cdots \quad \left\|\boldsymbol{\gamma}^N\right\|_u \right)^{\mathrm{T}} \tag{15}$$

where $\boldsymbol{\gamma}^n$ denotes the nth row of $\boldsymbol{\gamma}$. This formulation is equivalent to finding the sparsest solution, whereas the well known TSVD method tries to find the minimum energy solution (ℓ_2 norm minimization). The former allows the signal energy to be sharply localized whereas the latter makes the energy spatially spread out [31]. This is why CS inversion techniques always exhibit finer super resolution power than TSVD.

3.2. Computational Methods

Generally, the nonconvex $\ell_{u,0}$ minimization is addressed with some approximate techniques, e.g., greedy pursuit and $\ell_{u,1}$ convex relaxation, etc. [32]. A popular greedy pursuit method for MMV problem is called *modified orthogonal matching pursuit* (M-OMP) [30], or similarly, *simultaneous orthogonal matching pursuit* (S-OMP) [33]. The basic idea of M-OMP, which is quite similar to a well known super resolution technique named RELAX [34], is to iteratively refine the sparse solution along a local optimal path. One main drawback with these greedy methods is the poor super resolving ability. Therefore, we refer the readers to [30] and [33] for more details about M-OMP, and focus our discussion on $\ell_{u,1}$ relaxation method.

Rewriting (14) with a small revision on the objective function yields

$$\min \|\boldsymbol{\gamma}\|_{u,1} \quad \text{s.t.} \quad \|\mathrm{vec}\,(\mathbf{g} - \mathbf{A}\boldsymbol{\gamma})\|_2^2 \le \varepsilon^2 \tag{16}$$

This can be further regularized as

$$\tilde{\boldsymbol{\gamma}} = \arg\min_{\boldsymbol{\gamma}} \left(\|\boldsymbol{\gamma}\|_{u,1} + \lambda \|\mathrm{vec}\,(\mathbf{g} - \mathbf{A}\boldsymbol{\gamma})\|_2^2 \right) \tag{17}$$

Here the parameter $\lambda > 0$ is used to balance the two objectives and is well studied in [31]. However, the choice for u seems to be more various in literatures, e.g., $u = 1$ in [35], $u = 2$ in [30] and [36], and $u = \infty$ in [37] and [38]. We note that different selection usually produces significantly different results. Although a rigorous theoretical analysis of these choices is out of the scope of this paper, it is necessary for us to make a short discussion on them. Consider two typical choices, i.e., $u = 1$ and $u = 2$, respectively.

When $u = 1$, expanding (17) gives a clear insight to the choice

$$\tilde{\boldsymbol{\gamma}} = \arg\min_{\boldsymbol{\gamma}} \sum_{i=1}^{4} \left(\|\boldsymbol{\gamma}_i\|_1 + \lambda \|\mathbf{g}_i - \mathbf{A}\boldsymbol{\gamma}_i\|_2^2 \right) \tag{18}$$

Here $\boldsymbol{\gamma}_i$ and $\mathbf{g}_i$ denote the ith columns of $\boldsymbol{\gamma}$ and $\mathbf{g}$, respectively. Obviously, this is equivalent to applying CS inversion to each channel independently without any regards to the joint sparsity requirement.

When $u = 2$, the mixed norm operates along different polarization channels as ℓ_2 norm, and operates along different elevation position as ℓ_1 norm. The objective function seems to place more emphasis on the joint sparsity requirement. And this can be interpreted as follows. When an individual scatterer is located at different positions in different channels (for most cases, the differences are small, and the quadratic error term in (17) will not be affected too much), then the mixed norm term in (17) will be significantly increased from the l_2 norm to l_1 norm. Thus, to minimize the objective function, $\ell_{2,1}$ minimization tends to recover the signal with joint sparsity.

Therefore we prefer $\ell_{2,1}$ norm in PolSAR tomography. However, the results obtained with $\ell_{1,1}$ norm and M-OMP method will also be presented for comparison.

3.3. Performance Guarantees

Various criteria provide the guarantees for CS inversion performance, e.g., the spark, the null space property (*NSP*), and the restricted isometry property (*RIP*). For instance, the RIP theorem states that the recovery will be very stable if the matrix $\mathbf{A}$ satisfies the following condition

$$(1 - \delta_k) \|\mathbf{x}\|_2^2 \leq \|\mathbf{A}\mathbf{x}\|_2^2 \leq (1 + \delta_k) \|\mathbf{x}\|_2^2 , \tag{19}$$

where $\mathbf{x}$ is a vector with only k nonzero elements, and δ_k is a small value called *restricted isometry constant* (RIC). A smaller value of δ_k usually implies more stable results.

However, verifying these conditions is usually computationally too hard. And more seriously, due to the limited acquisition number in SAR tomography, it is sometimes impossible to satisfy these conditions (e.g., *RIP*). In such a case, the performance of these techniques is still unavailable, especially with respect to super resolution power and sidelobe suppression ability. As parts of this study, we will investigate and examine the performance of $\ell_{2,1}$ norm inversion technique through numerical simulations in the cases where RIP is not satisfied.

3.4. Signal Leakage Suppression

The main drawback with CS tomography is that the energy of individual scatterer may spill into the neighboring bins, resulting in some so-called outliers [23]. We call this *signal leakage*, and note that two main factors contribute to the problem:

1) Firstly, when inappropriate noise tolerance is set, i.e., quadratic error constraint is too strict, the measured data will be over fitted, and the individual scatterer may be approximated by several neighboring scatterers;
2) Secondly and more importantly, when the scatterer does not lie exactly at the sample gridding point s_n, i.e., there exists *basis mismatch*, the signal is incompressible in the identity basis matrix $\mathbf{I}$ (see, e.g., [24–26]), thus more than one coefficients in the recovered signal vector are required to well approximate each scatterer.

The analysis presented in [25] show that the error induced by such basis mismatch is well bounded and numerical simulations show 2–3 coefficients are usually enough to well approximate each scatterer. Hence, we propose here a window-based signal leakage suppression (SLS) algorithm.

Our basic strategy is to iteratively merge the neighboring coefficients. Firstly, we use the $\ell_{2,1}$ norm inversion technique to obtain

Table 1. Signal leakage suppression algorithm.

Step (1) Apply the CS inversion to the polarimetric data according to(14), producing the initial estimate for the reflectivity function $\tilde{\boldsymbol{\gamma}}$;
Step (2) Calculate the span image $\tilde{\boldsymbol{\gamma}}_{\text{span}} = \left\|\tilde{\boldsymbol{\gamma}}_{\text{HH}}\right\|^2 + \left\|\tilde{\boldsymbol{\gamma}}_{\text{HV}}\right\|^2 + \left\|\tilde{\boldsymbol{\gamma}}_{\text{VV}}\right\|^2$, and find the local maxima of the $\tilde{\boldsymbol{\gamma}}_{\text{span}}$. To suppress the small maxima caused by the noise, a thresholding operation is incorporated that only the maxima which exceed the threshold Th are preserved. Next, Put all the elevation values corresponding to the peaks, s_k, into a set Ω.
Step (3) Apply a window of width $nwin$, centered at $s_k \in \Omega$, to $\tilde{\boldsymbol{\gamma}}$ that all the coefficients out of the window are set to be zero, producing $\tilde{\boldsymbol{\gamma}}'$. Then, Synthesize a signal using $\tilde{\boldsymbol{\gamma}}'$ as $\mathbf{e}_i = \mathbf{A}\tilde{\boldsymbol{\gamma}}'$, and approximate $\mathbf{e}_i$ with single scatterer as $\tilde{s}_i = \arg\max_s \left\|(\mathbf{x}(s))^{\text{H}}\mathbf{e}_i\right\|_2$, where $\tilde{s}_i$ is the estimate for the scatterers' position, and $\mathbf{x}(s)$ is the steering vector of the scatterer with elevation value s.
Step (4) Upon all the scatterers' positions are obtained, the corresponding manifold $\mathbf{A}_0$ can be calculated, and the sparse reflectivity function can be estimated using LS criterion, $\tilde{\boldsymbol{\gamma}} = (\mathbf{A}_0^{\text{H}}\mathbf{A}_0)^{-1}\mathbf{A}_0^{\text{H}}\mathbf{g}$. Finally, the set Ω is updated by clearing its original elements and putting the updated elevation values into Ω.
Step (5) Repeat (3)–(4) until no change can be made.

the initial estimate for the reflectivity function $\tilde{\boldsymbol{\gamma}}$, and identify all the peaks in the polarimetric span image. The elevation values of these peaks are put into a set Ω. Then an iterative merging scheme begins: for each element $s_k \in \Omega$, a window centered at s_k, with a predefined width, is applied to $\tilde{\boldsymbol{\gamma}}$, and all the coefficients located in the window are merged, producing the estimates for the scatters' elevation values. Next, both $\tilde{\boldsymbol{\gamma}}$ and Ω are updated, and the iteration is repeated until no change can be made.

We presented the detailed SLS method in Table 1.

4. PERFORMANCE ANALYSIS

This section presents the results obtained by processing the simulated data to verify the effectiveness of the proposed CS tomography technique, which we call $\ell_{2,1}$-SLS method. Without loss of generality, our study is focused on the airborne case. The relevant parameters for the airborne are presented in Table 2. The radar system is assumed to be reciprocal so that only HH, HV, and VV channels are considered in the following simulations. All the data are supposed to be focused and co-registered in the range-azimuth plane in prior.

The parameters involved in the implementation of $\ell_{2,1}$-SLS are determined as follows. We use the noise tolerance $\varepsilon = \sqrt{3M}\sigma$ in the following simulations, as motivated by the investigation in [17] and [39]. However the original proposed value is multiplied by a factor $\sqrt{3}$, for the consideration of multichannel case in this study. The threshold involved in detecting the local maxima is $-20\,\mathrm{dB}$ relative to the largest local maximum, and the window size for SLS is $nwin = 0.2\rho_e$. Although a larger window may suppress the signal leakage better, it will reduce the super resolution power of the tomography technique more, on the other hand.

4.1. Single Scatterer Case

Presently, uniform sensor geometry is assumed, that is, ten sensors are uniformly distributed along the elevation direction with the sensor

Table 2. SAR platform parameters.

Parameters	Values	Unit
Carrier frequency	10	GHz
Slant range	8000	meters
Height	5000	meters

separation $\Delta b = 3\,\text{m}$, forming an aperture of 30 m. According to (5) and (7), the Fourier resolution ρ_e and ambiguity value L_a are 4 m and 40 m, respectively. The unknown reflectivity functions are sampled with $\varepsilon_s = 0.3\,m(\rho_e/10)$, and the corresponding gridding points are $-20, -19.7, \ldots 5.7, 6, \ldots 19.9$.

Consider a trihedral-like scatterer with unit amplitude located in the pixel of interest, that is, the scattering vector $\mathbf{k} = [1 \quad 0 \quad 1]$. Three cases are examined. Case 1: noise is absent, and $s = 6\,\text{m}$ (gridding point); Case 2: SNR = 15 dB, and $s = 6\,\text{m}$; Case 3: noise is absent,

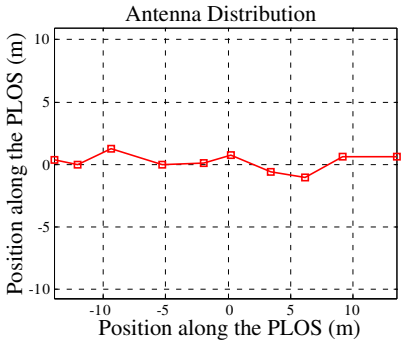

Figure 4. The antenna distribution plot.

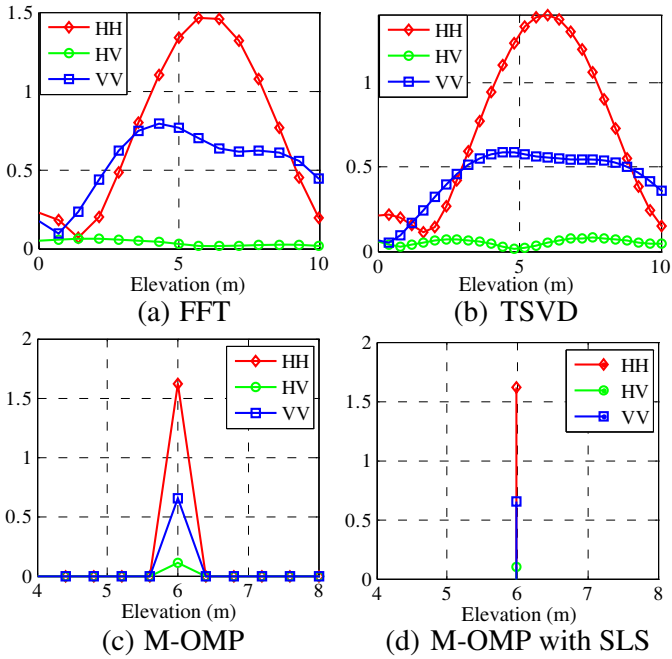

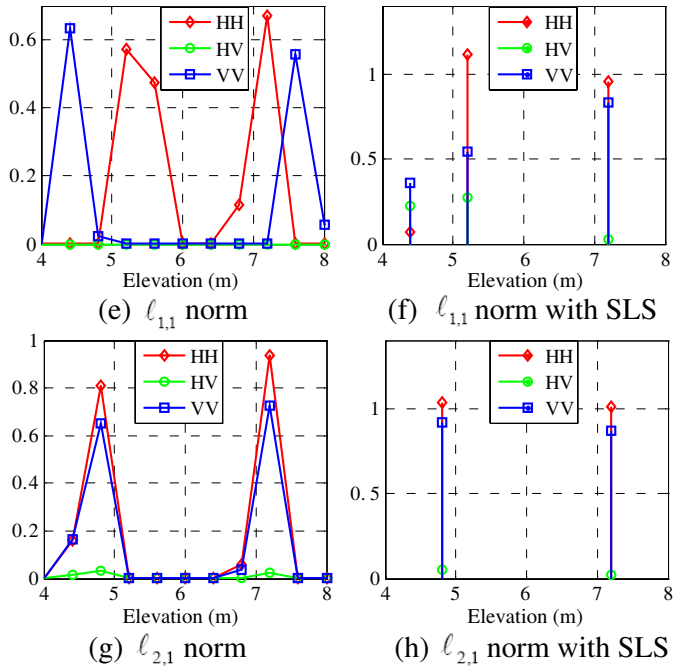

Figure 5. The elevation profiles of two closely separated scatterers ($\Delta s = 2\,\mathrm{m}$). (a) FFT method; (b) TSVD method; (c) M-OMP method; (d) M-OMP with signal leakage suppression; (e) $\ell_{1,1}$ minimization; (f) $\ell_{1,1}$ minimization with signal leakage suppression; (g) $\ell_{2,1}$ minimization; (h) $\ell_{2,1}$ minimization with signal leakage suppression.

but $s = 5.8\,\mathrm{m}$ (away from gridding point). Fig. 5 presents the results obtained with CS techniques. It can be seen that all four algorithms recover the signal perfectly in the first case. However, when noise or basis mismatch exists, signal leakage effect is obvious for both $\ell_{1,1}$ norm and $\ell_{2,1}$ norm inversions, that is, the scatterer energy spills to the neighboring bins, resulting in two scatterers. The M-OMP and $\ell_{2,1}$-SLS inversion algorithms both recover the scatterer quite accurately, and no significant difference between them can be observed in this single scatterer case.

4.2. Double Scatterers Case

We then study the double scatterers' case. Two scatterers are assumed to be separated in the elevation direction with the distance $\Delta s = 2\,\mathrm{m}$ ($s_1 = 5\,\mathrm{m}$, $s_2 = 7\,\mathrm{m}$), thus they can not be resolved with Fourier

beamforming method ($\rho_e = 4\,\mathrm{m}$). The corresponding scattering vectors are $\mathbf{k}_1 = [1 \quad 0 \quad 1]$ and $\mathbf{k}_2 = [1 \quad 0 \quad -1]$, respectively. The uniform sensor geometry is now relaxed by allowing a perturbation β on the sensor's position, $\beta \sim N\,(0, \Delta b/4)$, as presented in Fig. 4. The other parameters are the same as those in the previous simulations. Tomographic results obtained with FFT, TSVD and CS techniques are presented in Fig. 5. It can be seen that the FFT method and TSVD method can not separate the two scatterers at all. Although M-OMP method exhibits good performance in the single scatterer case, it now detects only one scatterer, $\tilde{s} = 6\,\mathrm{m}$, away from either of the two scatterers, showing poor super resolution ability.

Both $\ell_{1,1}$ norm and $\ell_{2,1}$ norm methods succeed in resolving the two scatterers, but the $\ell_{2,1}$ norm method shows better joint sparsity property than the $\ell_{1,1}$ norm method, i.e., the nonzero entries are more consistent in different channels for $\ell_{2,1}$ norm method. Again, signal leakage effect is observed for these two algorithms. After applying the SLS algorithm to $\ell_{2,1}$ norm, we obtain the results presented in Fig. 5(h),

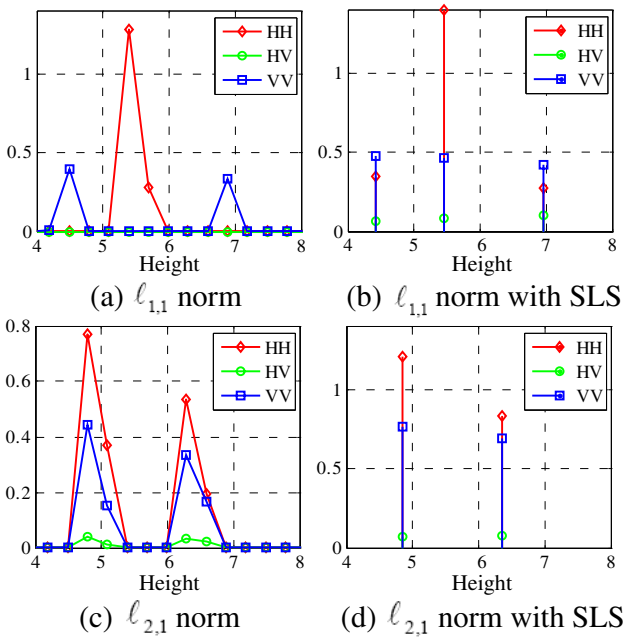

Figure 6. The elevation profiles of two closely separated scatterers ($\Delta s = 1.5\,\mathrm{m}$). (a) $\ell_{1,1}$ minimization; (b) $\ell_{1,1}$ minimization with signal leakage suppression; (c) $\ell_{2,1}$ minimization; (d) $\ell_{2,1}$ minimization with signal leakage suppression.

that is, $\tilde{s}_1 = 4.8\,\mathrm{m}$ and $\tilde{s}_2 = 7.2\,\mathrm{m}$. The results demonstrate the super resolution ability of $\ell_{2,1}$-SLS algorithm. Remember our discussion in Section 3 that $\ell_{1,1}$ norm method is equivalent to processing each polarimetric channel data separately. Hence, one may be interested in fusing the multichannel results together like the conventional polarimetric processing scheme. One such attempt is to applying our SLS algorithm to the $\ell_{1,1}$ norm results. However, the results are quite disappointing. Due to the poor joint sparsity property, the scatterer $s_2 = 5\,\mathrm{m}$ is wrong recognized as two close scatterers.

Another case further checks the performance of $\ell_{2,1}$-SLS algorithm (Fig. 6). With the other configurations unchanged, the two scatterers becomes even closer that $\Delta s = 1.5\,\mathrm{m}$ ($s_1 = 5\,\mathrm{m}$, $s_2 = 6.5\,\mathrm{m}$). In

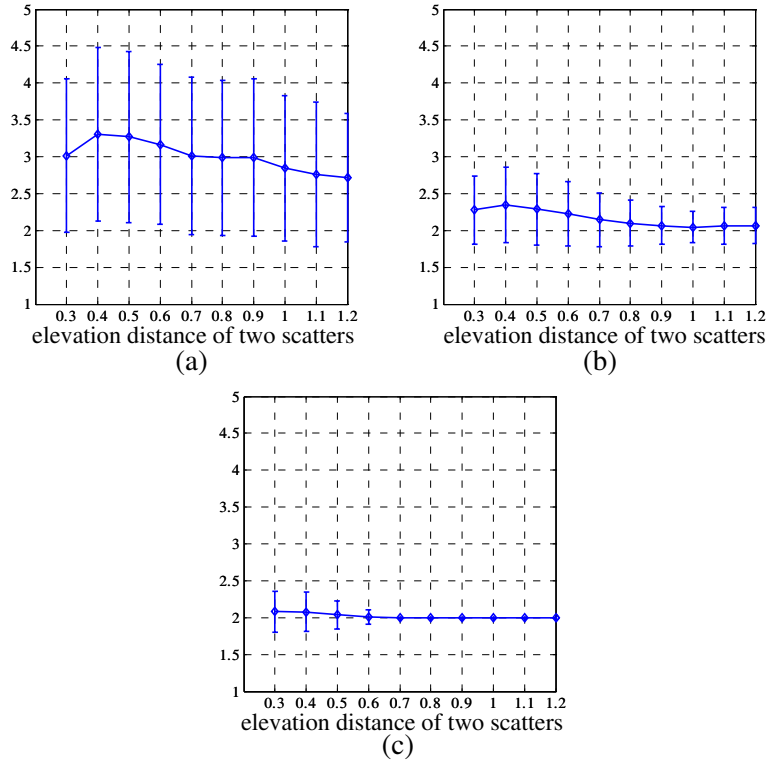

Figure 7. The average and standard deviation of the number of detected scatterers versus Δs, for different SNR. True scatterer number is $K = 2$. The distance Δs is normalized by ρ_e. (a) SNR $= 10\,\mathrm{dB}$. (b) SNR $= 15\,\mathrm{dB}$. (c) SNR $= 20\,\mathrm{dB}$.

this case, for $\ell_{1,1}$ norm method (independent processing), only one scatterer is detected in HH channel whereas two scatterers, both away from the true positions, are detected in VV channel. Fusing the results of all channels produces three scatterers. However, for $\ell_{2,1}$-SLS algorithm (joint processing), two scatterers with relative accurate estimate for the parameters are detected. The results verifies that polarimetric information can enhance the super resolution power of

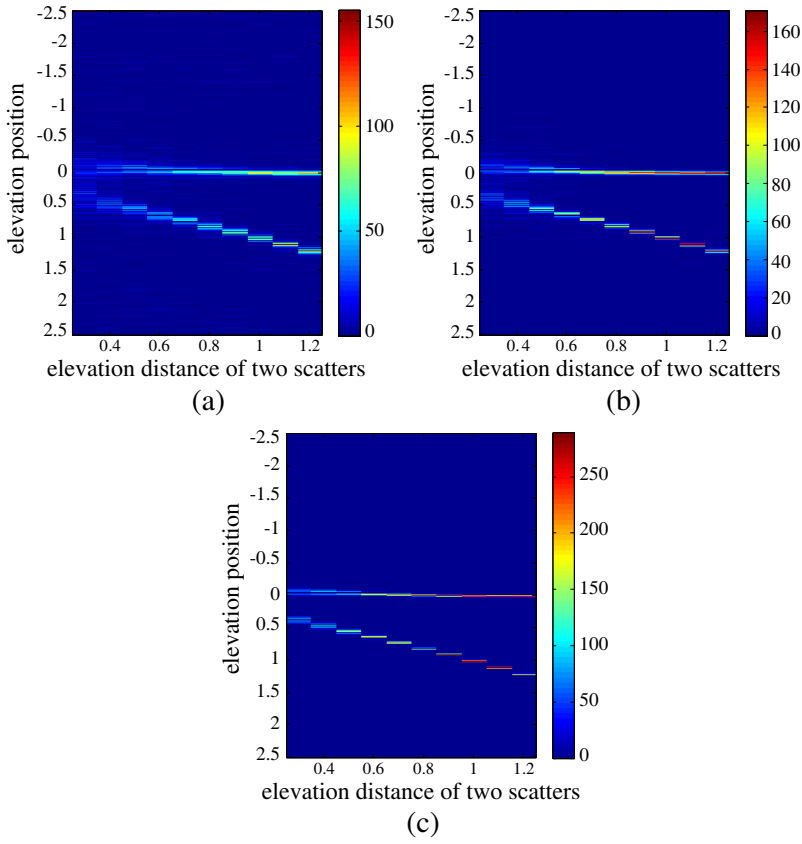

Figure 8. The spatial distribution of the detected scatterers versus Δs, for different SNR. True scatterer number is $K = 2$. The distance Δs and position estimates $\tilde{s}$. are all normalized by ρ_e. The image color is coded with the number of detected scatterers in the corresponding bin. When SNR gets higher or the elevation distance gets larger, the distribution get more concentrated, implying the estimates get more accurate. (a) SNR = 10 dB. (b) SNR = 15 dB. (c) SNR = 20 dB.

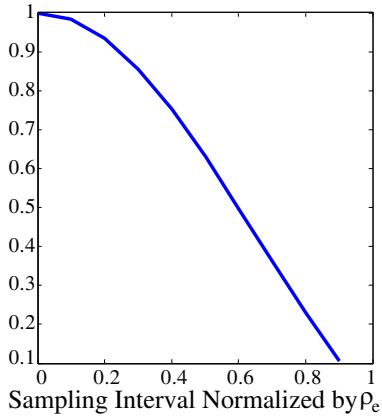

Figure 9. The RIC value δ_k $(k = 2)$ versus the normalized sampling interval. In our study, the sampling interval is $\varepsilon_s = \rho_e/10$, thus the corresponding RIC is about 0.98.

the CS inversion, and joint processing scheme possesses better super resolution power than the conventional polarimetric processing scheme.

We then investigate the performance of $\ell_{2,1}$-SLS algorithm versus Δs. Three typical SNR are considered, i.e., SNR = 10 dB, 15 dB and 20 dB. Two scatterers are assumed, $s_1 = 0$ and $s_2 = \Delta s$, with Δs ranging from $0.3\rho_e$ to $1.2\rho_e$ ($\Delta s = 0.3\rho_e$, $0.4\rho_e$, ...). For each combination of Δs and SNR, 500 Monte Carlo runs are carried out. Fig. 7 presents the average and standard derivation of the number of detected scatterers. And Fig. 8 presents the spatial distribution of the detected scatterers. It can be seen that when SNR = 10 dB, $\Delta s \geq 0.5\rho_e$ is required to well resolve the two scatterers. When the SNR is greater than 15 dB, even the scatterers with distance $\Delta s = 0.3\rho_e$ can be separated with high probability. We note that although the RIC is quite big for this case, RIC = 0.98 (see Fig. 9), the results are quite satisfactory. It should be mentioned that the results don't mean the RIP theorem is violated, but show that RIC may not be appropriate to predict the tomography performance. And this can be interpreted as follows. The RIP theorem measures the estimating error by calculating the difference between $\boldsymbol{\gamma}$ and $\tilde{\boldsymbol{\gamma}}$ in element wise manner. So if you don't locate the scatter in the desired entry, the error will be quite serious, implying the inversion is not "stable". However, in SAR tomography, we don't need to locate the scatterer within the element precision. So even if the total error predicted by the RIP theorem is quite serious, the tomographic results may be satisfactory.

4.3. Performance in the Case with Reduced Acquisition Number

It highly concerns the community of SAR tomography that how many acquisitions or tracks at least are required to achieve the desired resolution without bringing serious sidelobe problem. When the acquisition number is limited, a small sensor separation will produce poor super resolving ability, while a large sensor separation may bring serious sidelobe problem. In [40], the question is studied for the MUSIC method by using the prolate spheroidal wave functions. In this study, we show that, for the $\ell_{2,1}$-SLS method, the minimum number requirement (8) can be greatly reduced if appropriate data acquisition geometry is designed. Also we will show that the uniform sampling is generally not the best option for CS inversion technique.

Consider the situation that ten sensors are distributed along the elevation direction with the sensor separation $\Delta b = 3\,\mathrm{m}$. Also a perturbation, $\beta \sim N(0, \Delta b/4)$, is allowed for the antenna position. The nominal resolution is $\rho_e = 4\,\mathrm{m}$, and the ambiguity value is $L_a = 40\,\mathrm{m}$, with the unambiguous elevation value $s \in [-20,\ 20)$. However we try to reconstruct the elevation profile with only five sensors chosen from the whole set, and three cases are studied. The first one is a nonuniform sampling case with sensors $\{1, 2, 5, 7, 10\}$, and both the second and the third are uniform sampling cases, with sensors $\{1, 2, 3, 4, 5\}$ and $\{1, 3, 5, 7, 9\}$, respectively. Fig. 10 presents the sensor distribution for the three cases. Since it is expected that a serious ambiguity problem would happen for a high elevation value, e.g., $s = 15\,\mathrm{m}$, we assume the scatterers are located around this position. The SNR is supposed to be 15 dB.

Both single scatterer ($s = 15\,\mathrm{m}$, $\mathbf{k} = [1 \quad 0 \quad 1]$) and double scatterers case ($s_1 = 15\,\mathrm{m}$, $s_2 = 13\,\mathrm{m}$, $\Delta s = \rho_e/2$, $\mathbf{k}_1 = [1 \quad 0 \quad 1]$, $\mathbf{k}_2 = [1 \quad 0 \quad -1]$) are studied, and the results obtained with TSVD and $\ell_{2,1}$-SLS methods are presented in Fig. 11 and Fig. 12, where 100 Monte Carlo runs are carried out for each case. It can be seen that $\ell_{2,1}$-SLS method exhibits much lower ambiguity level and

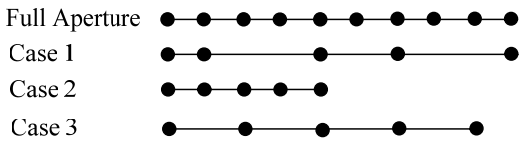

Figure 10. The sensor distribution for the cases with reduced acquisition number.

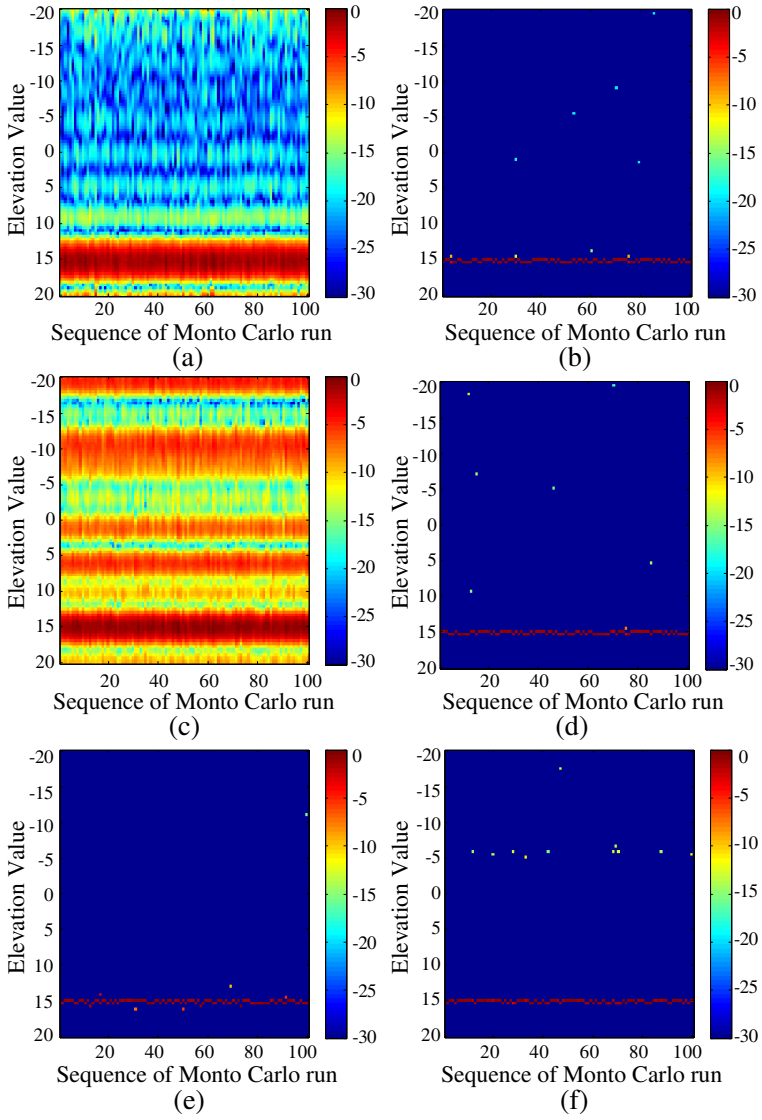

Figure 11. The elevation profiles for single scatterer. For each case, 100 Monte Carlo runs are carried out. The image color is coded with the span intensity of the detected scatterers (in decibel unit), and the intensity is normalized by the maximum. SNR = 15 dB. (a) TSVD with ten sensors. (b) $\ell_{2,1}$-SLS with ten sensors. (c) TSVD with sensors $\{1, 2, 5, 7, 10\}$. (d) $\ell_{2,1}$-SLS with sensors $\{1, 2, 5, 7, 10\}$. (e) $\ell_{2,1}$-SLS with sensors $\{1, 2, 3, 4, 5\}$. (f) $\ell_{2,1}$-SLS with sensors $\{1, 3, 5, 7, 9\}$.

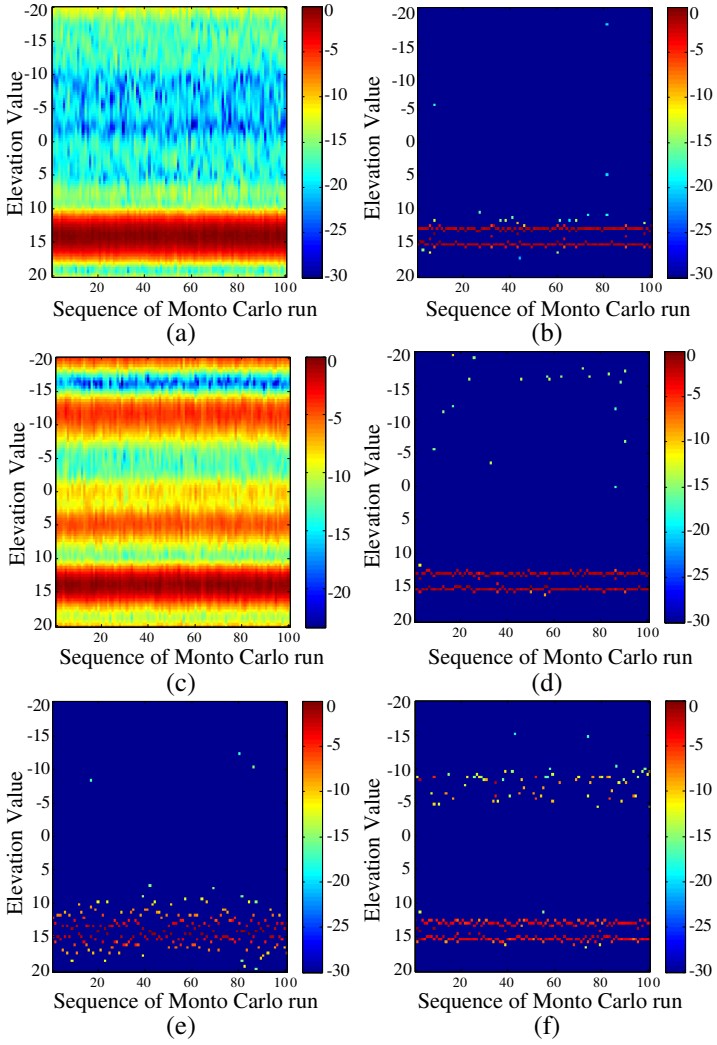

Figure 12. The elevation profiles for two closely separated scatterers. For each case, 100 Monte Carlo runs are carried out. The image color is coded with the span intensity of the detected scatterers (in decibel unit), and the intensity is normalized by the maximum. SNR = 15 dB. (a) TSVD with ten sensors. (b) $\ell_{2,1}$-SLS with ten sensors. (c) TSVD with sensors $\{1, 2, 5, 7, 10\}$. (d) $\ell_{2,1}$-SLS with sensors $\{1, 2, 5, 7, 10\}$. (e) $\ell_{2,1}$-SLS with sensors $\{1, 2, 3, 4, 5\}$. (f) $\ell_{2,1}$-SLS with sensors $\{1, 3, 5, 7, 9\}$.

finer super resolving ability than TSVD for both cases. When only five sensors are used, the results with sensors $\{1, 2, 3, 4, 5\}$ show significantly reduced super resolution power [see Fig. 12(e)], and the results with sensors $\{1, 3, 5, 7, 9\}$ exhibit serious sidelobe or ambiguity problem [see Fig. 11(f) and Fig. 12(f)]. It is interesting that no obvious performance deterioration can be observed in the nonuniform sampling case, compared to the results using all sensors. Its performance superiority over the uniform sampling case can be interpreted as follows: the small separation between some sensors helps to suppress the sidelobe while the total long aperture length helps to improve the super resolution power. And thanks to the sparsest solution pursuit strategy in CS techniques, the above two advantages can be enjoyed simultaneously.

Hence, for a practical system which wants to achieve a desired resolution with limited acquisition number and without serious sidelobe problem, nonuniform sensor geometry is a good choice, and it can be designed as follows: we first design a uniform sensor array up to our requirement, and then nonuniformly extract some sensors to form the required sensor geometry. The most important thing is to keep several sensors close enough to suppress the sidelobe and then to make the total baseline span as long as possible.

5. CONCLUSION

In this paper, we propose a mixed norm sparse reconstruction method for jointly processing multibaseline PolSAR data and propose a window based iterative algorithm for signal leakage suppression. The tomography technique based on these two algorithms is named $\ell_{2,1}$-SLS, and we examine its performance with exhaustive simulations. The basic conclusions are presented as follows:

(1) Polarimetric measurements do help to improve the resolving ability. Two scatterers, which can not be separated in single polarization image, may be resolved in multi-polarimetric case, if they possess significant difference in scattering mechanism;

(2) Compared to the results obtained by processing each polarimetric channel data independently, the results obtained with joint processing scheme ($\ell_{2,1}$-SLS) show much better joint sparsity property. And the joint sparsity property highly avoids the work of matching the scatterers in different channels, and also reduce the possibility of misestimating the scatterer number;

(3) Signal leakage will be obvious when basis mismatch exists or the noise tolerance is inappropriately set. The proposed SLS

algorithm works well for both single scatterer and two closely separated scatterers situations;

(4) Generally, the $\ell_{2,1}$-SLS method show better super resolution power than TSVD, M-OMP, and the $\ell_{1,1}$ relaxation method. Monte Carlo Simulations show that when the acquisition number $M = 10$, SNR $= 15\,\text{dB}$, two scatterers with $\Delta s = 0.3\rho_e$ can be resolved with high probability. RIC value may be not critical in predicting the $\ell_{2,1}$-SLS performance. Even with a big RIC value, the tomography results obtained by $\ell_{2,1}$-SLS may be satisfactory;

(5) The minimum acquisition number for $\ell_{2,1}$-SLS can be greatly reduced without obvious loss in super resolving ability or bringing serious sidelobe problem, if appropriate sensor geometry is designed. Nonuniform sensor geometry exhibits remarkable superiority than uniform geometry, i.e., the former can enjoy the super resolving ability and the low ambiguity level of CS techniques simultaneously.

REFERENCES

1. Lazaro, A., D. Girbau, and R. Villarino, "Simulated and experimental investigation of microwave imaging using UWB," *Progress In Electromagnetics Research*, Vol. 94, 263–280, 2009.
2. Guo, D., H. Xu, and J. Li, "Extended wavenumber domain algorithm for highly squinted sliding spotlight SAR data processing," *Progress In Electromagnetics Research*, Vol. 114, 17–32, 2011.
3. Zhang, M., Y. W. Zhao, H. Chen, and W.-Q. Jiang, "SAR imaging simulation for composite model of ship on dynamic ocean scene," *Progress In Electromagnetics Research*, Vol. 113, 395–412, 2011.
4. Cumming, I. G. and F. K. Wong, *Digital Processing of Synthetic Aperture Radar Data: Algorithm and Implementation*, Artech House, 2005.
5. Zandoná Schneider, R., K. P. Papathanassiou, I. Hajnsek, and A. Moreira, "Polarimetric and interferometric characterization of coherent scatterers in urban areas," *IEEE Trans. Geosci. Remote Sens.*, Vol. 44, 971–984, 2006.
6. Wu, B.-I., M. C. Yeuing, Y. Hara, and J. A. Kong, "InSAR height inversion by using 3-D phase projection with multiple baselines," *Progress In Electromagnetics Research*, Vol. 91, 173–193, 2009.
7. Hanssen, R., *Radar Interferometry: Data Interpretation and Error Analysis*, Kluwer Academic, Dordrecht, the Netherlands, 2001.

8. Liu, Q., S. Xing, X. Wang, J. Dong, D. Dai, and Y. Li, "The slope effect of coherent transponder in InSAR," *Progress In Electromagnetics Research*, Vol. 127, 351–370, 2012.
9. Liu, Q., S. Xing, X. Wang, J. Dong, D. Dai, and Y. Li, "The interferometry phase of InSAR coherent jamming with arbitrary waveform modulation," *Progress In Electromagnetics Research*, Vol. 124, 101–118, 2012.
10. Krieger, G., I. Hajnsek, K. P. Papathanassiou, M. Younis, et al., "Interferometric synthetic aperture radar (SAR) missions employing formation flying," *Proceeding of IEEE*, Vol. 98, 816–843, 2010.
11. Felguera-Martín, D., J.-T. González-Partida, P. Almorox-González, M. Burgos-García, and B.-P. Dorta-Naranjo, "Interferometric inverse synthetic aperture radar experiment using an interferometric linear frequency modulated continuous wave millimeter-wave radar," *IET Radar Sonar Navig.*, Vol. 5, 39–47, 2011.
12. Cloude, S. R., "Polarization coherence tomography," *Radio Sci.*, Vol. 41, 4017, 2006.
13. Reigber, A. and A. Moreira, "First demonstration of airborne SAR tomography using multibaseline L-band data," *IEEE Trans. Geosci. Remote Sens.*, Vol. 38, 2142–2152, 2000.
14. Fornaro, G., D. Reale, and F. Serafino, "Four-dimensional SAR imaging for height estimation and monitoring of single and double scatterers," *IEEE Trans. Geosci. Remote Sens.*, Vol. 47, 224–237, 2009.
15. Zhu, X. and R. Bamler, "Very high resolution spaceborne SAR tomography in urban environment," *IEEE Trans. Geosci. Remote Sens.*, Vol. 48, 4296–4307, 2010.
16. Zhu, X. and R. Bamler, "Tomographic SAR inversion by L_1-norm regularization — The compressive sensing approach," *IEEE Trans. Geosci. Remote Sens.*, Vol. 48, 3939–3846, 2010.
17. Budillon, A., A. Evangelista, and G. Schirinzi, "Three-dimensional SAR focusing from multipass signal using compressive sampling," *IEEE Trans. Geosci. Remote Sens.*, Vol. 49, 488–499, 2011.
18. Sauer, S., L. Ferro-Famil, A. Reigber, and E. Pottier, "Three-dimensional imaging and scattering mechanism estimation over urban scenes using dual-baseline polarimetric InSAR observations at L-band," *IEEE Trans. Geosci. Remote Sens.*, Vol. 49, No. 11, 4616–4629, Nov. 2011.

19. Nannini, M., R. Scheiber, R. Horn, and A. Moreira, "First 3-D reconstructions of targets hidden beneath foliage by means of polarimetric SAR tomography," *IEEE Geosci. Remote Sens. Letters*, Vol. 9, No. 1, 60–64, 2012.
20. Austin, C. D., E. Ertin, and R. L. Moses, "Sparse signal methods for 3-D radar imaging," *IEEE J. Sel. Topics in Signal Process.*, Vol. 5, 408–423, 2011.
21. Frey, O. and E. Meier, "Analyzing tomographic SAR data of a forest with respect to frequency, polarization, and focusing technique," *IEEE Trans. Geosci. Remote Sens.*, Vol 49, No. 10, 3648–3659, 2011.
22. Tebaldini, S., "Algebraic synthesis of forest scenarios from multibaseline PolInSAR data," *IEEE Trans. Geosci. Remote Sens.*, Vol. 47, 4132–4142, 2009.
23. Zhu, X. and R. Bamler, "Super-resolution power and robustness of compressive sensing for spectral estimation with application to spaceborne tomographic SAR," *IEEE Trans. Geosci. Remote Sens.*, Vol. 50, No. 1, Jan. 2012.
24. Chi, Y., L. L. Scharf, A. Pezeshki, and A. R. Calderbank, "Sensitivity to basis mismatch in compressed sensing," *IEEE Trans. Signal Process.*, Vol. 59, 2182–2195, 2011.
25. Herman, M. A. and T. Strohmer, "General deviants: An analysis of perturbations in compressed sensing," *IEEE J. Sel. Topics in Signal Process.: Special Issue on Compressive Sens.*, Vol. 4, 342–349, 2010.
26. Herman, M. A. and D. Needell, "Mixed operators in compressed sensing," *Proc. 44th Ann. Conf. Inf. Sci. Syst. (CISS)*, Princeton, NJ, 2010.
27. Aguilera, E., M. Nannini, and A. Reigber, "Multi-signal compressed sensing for polarimetric SAR tomography," *IEEE International Geoscience and Remote Sensing Symposium (IGARSS)*, 1369–1372, 2011.
28. Donoho, D., "Compressed sensing," *IEEE Trans. Inf. Theory*, Vol. 52, 1289–1306, 2006.
29. Candès, E. and M. B. Wakin, "An introduction to compressive sampling," *IEEE Signal Process. Mag.*, Vol. 25, 21–30, 2008.
30. Cotter, S. F., D. Rao, K. Engan, and K. Kreutz-Delgado, "Sparse solutions to linear inverse problems with multiple measurement vectors," *IEEE Trans. Signal Process.*, Vol. 53, 2477–2488, 2005.
31. Chen, S., D. Donoho, and M. Saunders, "Atomic decomposition by basis pursuit," *SIAM J. Sci. Comput.*, Vol. 20, 33–61, 1998.

32. Tropp, J. A. and S. J. Wright, "Computational methods for sparse solution of linear inverse problem," *Proceeding of IEEE*, Vol. 98, 948–958, 2010.
33. Tropp, J. A., A. C. Gilbert, and M. J. Strauss, "Algorithms for simultaneous sparse approximation. Part I: Greedy pursuit," *Signal Processing (Special Issue on Sparse Approximations in Signal and Image Processing)*, Vol. 86, 572–588, 2006.
34. Li, J. and P. Stoica, "Efficient mixed-spectrum estimation with applications to target feature extraction," *IEEE Trans. Signal Process.*, Vol. 44, 281–295, 1996.
35. Chen, J. and X. Huo, "Theoretical results on sparse representations of multiple-measurement vectors," *IEEE Trans. Signal Process.*, Vol. 54, 4634–4643, 2006.
36. Malioutov, D. M., M. Cetin, and A. S. Willsky, "A sparse signal reconstruction perspective for source localization with sensor arrays," *IEEE Trans. Signal Process.*, Vol. 53, 3010–3022, 2005.
37. Tropp, J. A., "Algorithms for simultaneous sparse approximation. Part II: Convex relaxation," *Signal Process. (Special Issue on Sparse Approximations in Signal and Image Processing)*, Vol. 86, 589–602, 2006.
38. Negahban, S. N. and M. J. Wainwright, "Simultaneous support recovery in high dimensions: Benefits and perils of block," *IEEE Trans. Inf. Theory*, Vol. 57, 3841–3863, 2011.
39. Candès, E., "Compressive sampling," *Proc. Int. Congr. Math.*, Vol. 3, 1433–1452, Madrid, Spain, 2006.
40. Nannini, M., R. Scheiber, and A. Moreira, "Estimation of the minimum number of tracks for SAR tomography," *IEEE Trans. Geosci. Remote Sens.*, Vol. 47, 531–543, 2009.